PRESSURE PROFILE MEASUREMENTS WITHIN THE GAS FILM OF JOURNAL FOIL BEARINGS USING AN INSTRUMENTED ROTOR WITH TELEMETRY

K. Shalash, J. Schiffmann
Laboratory for Applied Mechanical Design
École Polytechnique Fédérale de Lausanne
Neuchâtel 2000, Switzerland

ABSTRACT

Foil bearings are strong candidates to support oil-free turbomachinery. Although foil bearings are a widely used technology, models describing their behavior are not validated using the film pressure, which is the fundamental variable of any fluid film bearing. This paper presents pressure profiles measured within the gas film of a journal foil bearing. The pressure is measured using an instrumented rotor with embedded pressure probes and wireless telemetry. The measurements yield the simultaneous circumferential pressure profiles at two axial positions inside the bearing. Proximity probes on the bearing allowed the measurement of the corresponding rotor orbits. The bearing under investigation is a bump type compliant journal bearing, with a nominal diameter of 40mm, an L/D = 1, and was tested up to 37.5 krpm. Load-displacement and break-away tests were performed on the test bearing in order to identify bearing parameters necessary for reproducibility. The pressure profiles are compared to a frequency domain foil bearing model. This paper is a step towards further fundamental understanding of the foil bearing behavior, and the validation of the rich modelling literature.

INTRODUCTION

Gas lubricated foil bearings showed competency in several high-speed turbomachinery applications. The bearings are categorized as self-acting (dynamic) gas lubricated fluid film bearings. They are constructed of three main components: (i) a top foil, which along with the rotor creates the aerodynamic wedge necessary for generating load capacity, (ii) a bump foil, which is serving as a compliant structure beneath the top foil, and (iii) a sleeve, where the bump and top foils are fixed. At the start of the machine, the rotor is in mechanical contact with the top foil, and at a given speed the rotor is rotating fast enough to yield enough pressure within the fluid film to lift-off the top foil. The strength of the foil bearing technology stems from their high load capacity, tolerance to misalignment and thermal gradients, soft failure attributes, and oil-free capabilities. The foil bearing technology is currently integrated in several applications where speed, high temperature, low maintenance requirements, and oil contamination are of paramount importance. These applications include air cycle machines [1], gas turbines [2], turbopumps [3], turbocompressors [4], and turbochargers [5].

In terms of first principles, a running foil bearing incorporates different physical phenomena. Fluid dynamics govern the gas film pressure, heat transfer and thermodynamics govern the thermal gradients within the bearing, and structural mechanics govern the compliance of the underlying structure (the bump foil). The interaction between the flow field, the thermal field, and the structure boils down to a complex fluid-structure-interaction problem that governs the gas film inside the bearing, and the deflection of the foils. Moreover, the solution to this problem governs the dynamic coefficients of the bearing (stiffness and damping), which in turn would dictate the rotor dynamics.

Given the complexity and the coupling of the different physical phenomena involved in the operation of a gas foil journal bearing (GFJB), modelling such system is a tedious task. But most importantly, measuring basic quantities like the gas film pressure, temperature, and thickness, as well as the foil deflection is very difficult to execute [6]. The absence of these measurements hinders the conclusive validation of foil bearing models. This lack of internal measurements is consequently obstructing the complete understanding and the identification of the root cause of foil bearing problems based on scientifically backed empirical evidence. That being said, and given the fact that foil bearing technologies are already integrated in several market products [1], it seems as if the foil bearing development path jumped several initial steps due to the complexity of the required measurements.

Considering the Technology Readiness Levels (TRL) scale developed by NASA in the 1980s, each newly developed technology shall pass through different phases of development with a precise exit criteria [7]. The scale starts with TRL-1, which is dedicated for basic principles observation and reporting; and ends with TRL-9, which is the actual successful mission operation. The TRL scale is currently widely used by several technology development institutions including government and industry.

Foil bearings can be considered a TRL-9 technology. However, they lack experimentally validated models, which is a consequence of the lack of experimental gas film measurements. At this point, it is worth mentioning that the majority of the experimental effort on foil bearings is either a proof of concept for a machine supported on foil bearings (i.e. ability to run heavy rotors, small rotors, fast, or hot applications), or studying high level performance metrics (i.e. dynamic response, lift-off speed, startup torque, and structural stiffness and damping).

A better fundamental understanding of the basic quantities governing the performance of foil bearings is required to push the boundaries and the limitations of the foil bearing technology. This requires further research at TRL-1, and 2. Such endeavor will eventually allow running heavier, faster, and hotter turbomachines.

NOMENCLATURE

GFJB	Gas foil journal bearing
TRL	Technology readiness level
PTFE	Polytetrafluoroethylene

L	Bearing length
D	Bearing diameter
J_{rot}	Test rotor inertia
J_{mot}	Motor inertia
J_{coup}	Coupling inertia
$\dot{\omega}$	Deceleration
T_{FB}	Foil bearing friction torque
T_{REB}	Roller element bearing friction torque
$T_{windage}$	Motor windage torque
$\bar{z}$	Axial bearing position (D/2L)
P	Pressure
P_{amb}	Ambient pressure
θ	Circumferential bearing angle

REVIEW OF THE LITERATURE

The literature attempting the measurement of fluid film variables in gas foil bearings (pressure and thickness) is limited to the NASA report by Ruscitto et al. [6]. The authors planned to simultaneously measure the pressure and the film thickness inside an operating foil journal bearing. The bearing under investigation was of the bump type, with one bump foil (360°), and one overlaid top foil, which were both made out of Inconel X-750 for the purpose of the intended application (gas turbine engine). The authors adopted a floating bearing configuration, where the test rotor was supported on roller element bearings and was driven by a turbine. The rotor was instrumented with custom made gap and pressure sensors to measure the circumferential profiles inside an overhung floating test foil bearing. The sensors were powered and their signal was transmitted using a slip ring assembly. The fluid film profiles were measured at different loads (up to 200 N), and speeds (up to 60 krpm).

Ruscitto et al. [6] were unsuccessful in measuring the pressure profiles, due to the cutoff frequency of the used pressure sensor, which was essentially a proximity probe that measured the deflection of a flexible membrane. The authors confirmed the flawed pressure measurement by testing their instrumented rotor on a plane gas bearing with a static pressure tap. The comparison was not in favor of continuing the pressure measurement campaign.

The film thickness measurements were successful, and were compared to a foil bearing model. The comparison yielded a large discrepancy between measurement and simulation, with an underestimation of the gas film thickness, a corresponding overestimation in the pressure profile within the gas film can be deduced. Three decades later, San Andrés and Kim [8] attempted a second comparison with the measured film thickness using foil bearing model that takes into account the elasticity of the top foil. The authors were not satisfied by the clearance definition and value given by Ruscitto et al. [6] for their test bearing, and hence, chose a clearance value that matches the measured minimum film thickness. Even with this modeling approach, the model presented was only able to capture the location and the value of the minimum film thickness inside the bearing, the rest of the profile was significantly underestimated. These results clearly suggest that a significant gap exists between experimental data and GFJB models.

GOAL AND OBJECTIVES

The goal of this paper is to address the lack of experimental data hindering the conclusive validation of foil bearing models. In order to attain this goal the following objectives are defined:

1. Designing and building of a test-rig capable of testing foil bearings beyond their liftoff speeds, and up to the instability thresholds of the rotors.
2. Designing and prototyping of an instrumented rotor capable of measuring the pressure within the gas film of foil bearings.
3. Manufacture serviceable journal foil bearings, and perform the necessary tests to identify them.
4. Measuring the pressure within the gas film of journal foil bearings.
5. Compare the measurements to a foil bearing model.

TEST RIG AND INSTRUMENTED ROTOR

The test rig used in this experimental campaign consists of an electric motor that drives an instrumented rotor with embedded pressure probes and a wireless telemetry system - Figure 1. The instrumented rotor is supported on two GFJBs. The non-drive end

bearing (far from the coupling) is considered the test bearing. Each bearing is equipped with two orthogonal proximity capacitive probes for rotor orbital measurements (uncertainty ± 1.3%, range 350 µm).

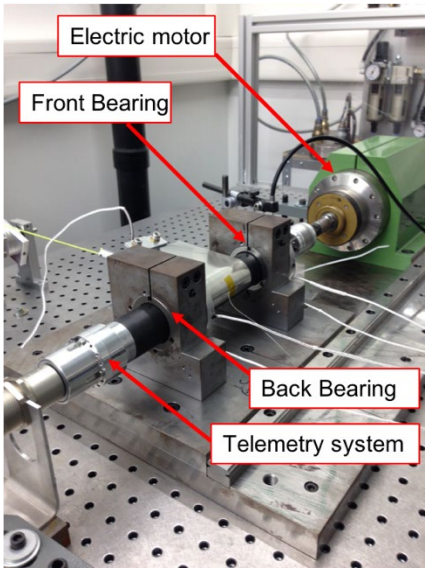

Figure 1 - Photograph of the test rig showing the electric motor, the flexible coupling, and the instrumented rotor supported on two GFJBs. The rotor is wrapped with a foil under tension between the two foil bearings for loading purposes.

The instrumented rotor consists of two embedded temperature compensated pressure probes at the same circumferential position for simultaneous measurements. A wireless telemetry system is used to power the pressure probes using an induction system, and transmit the measured signal using an RF transmitter. Details on the measurement system are presented in an accompanying paper [9].

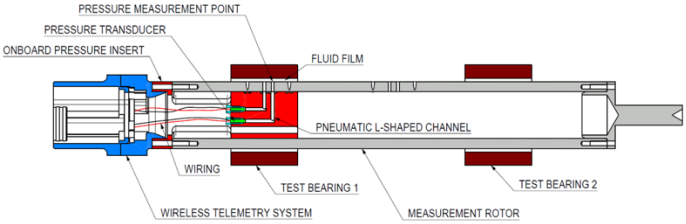

Figure 2 - Sketch of the instrumented rotor highlighting the embedded pressure measurement probes and the wireless telemetry system.

An auxiliary setup is used for load-displacement measurement. The mechanism exerts gradual load to the on the rotor, and the corresponding displacement is measured using proximity probes. Details on the mechanism can be found in [10].

A second auxiliary setup is developed to measure the breakaway torque in foil bearings - Figure 3, which allows the deduction of the foil bearing preload in order to characterize and compare different foil bearings, as well as facilitate reproducibility. In this setup a mockup rotor is used with the same diameter and surface coating as the actual test-rotor. The test foil bearing is held inside a bearing holder that is assembled to surround the mockup rotor. The bearing holder is connected to a torque arm in order to impose a normal load that is measured with a load cell. A second torque arm is connected to the mockup rotor in order to introduce a rotational torque, which is measured with a second load cell – knowing the length of the torque arm. A proximity probe is simultaneously measuring the position of the torque arm. At the moment of abrupt change in position the measured torque is considered the break-away torque.

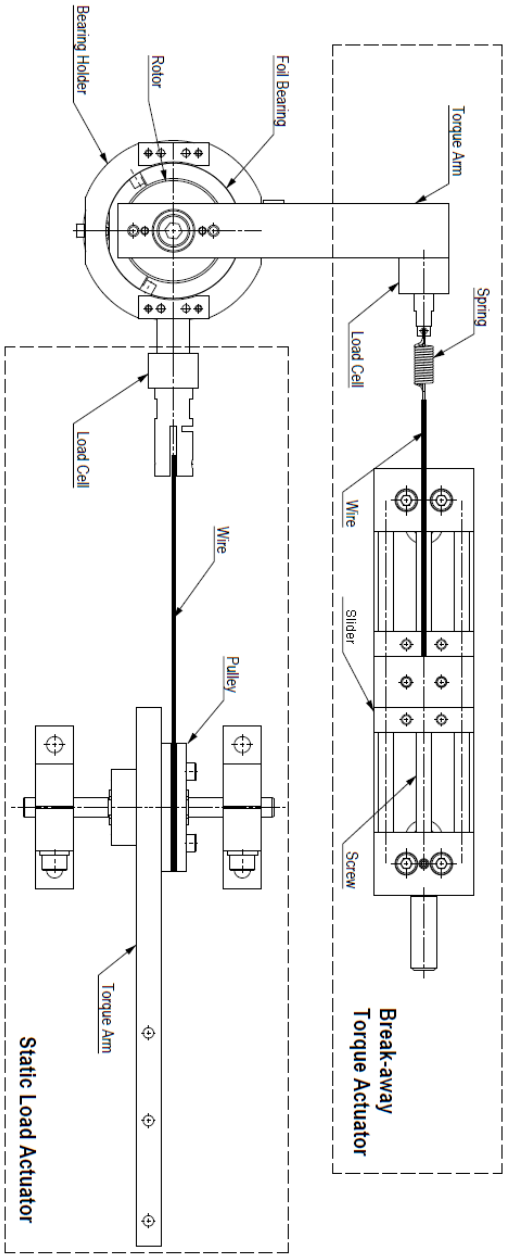

Figure 3 - Top view schematic of the break-away torque auxiliary setup.

DESCRIPTION OF BEARING UNDER INVESTIGATION

The GFJB under investigation -Figure 4- is of the sinusoidal type described in a previous work by the authors [10,11]. The bearing has 3 stainless steel bump foil pads (120°), and 1 continuous stainless steel top foil coated with PTFE. In order to adjust the assembly clearance of the bearing, round metal shims (top foil) are used to reduce the clearance. The bearing's nominal diameter is 40 mm, with an L/D = 1.

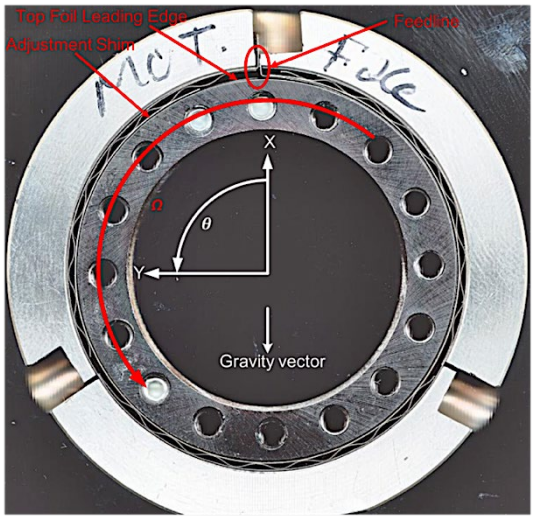

Figure 4 - Photograph of the actual test foil bearing under investigation highlighting the location of the feedline, the direction of rotation, and the angular reference.

Metrology. The test bearing was measured with an inner bore probe in order to identify the circularity of the bearing under investigation. The measurements showed more than 300 µm (peak-peak) of runout error. Figure 5 shows the measured circularity profile in the bearing center. Such deviations are expected to significantly influence the pressure profile measurements and to affect the dynamic bearing properties [10]. The bearing inner diameter was also measured at 3 points (60°) using a precision dimensional measurement machine. The measurements were executed at a constant maximum load of 10 grams, yielding the following diameters: 39.50, 39.44, and 39.29 mm, hence, confirming the lack of circularity of the foil bearing. Given that rotor diameter is 39.37 mm, the measured bearing diameters yields clearance values of 0.065, 0.035, and -0.04 mm.

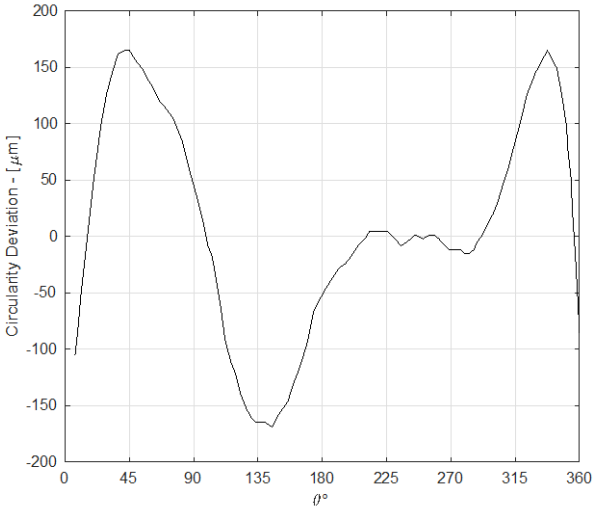

Figure 5 - Circularity deviation measured in the middle of the foil bearing under investigation.

Load-Displacement. The load-displacement auxiliary setup is used to identify the load-displacement characteristics of the GFJB under investigation. The curves suggest a relatively high preload, as no apparent displacement occurs at no load - Figure 6. Hence, the bump foils are immediately engaged at the onset of displacement. The typical hysteresis loop is observed signaling the existence of Coulomb friction damping.

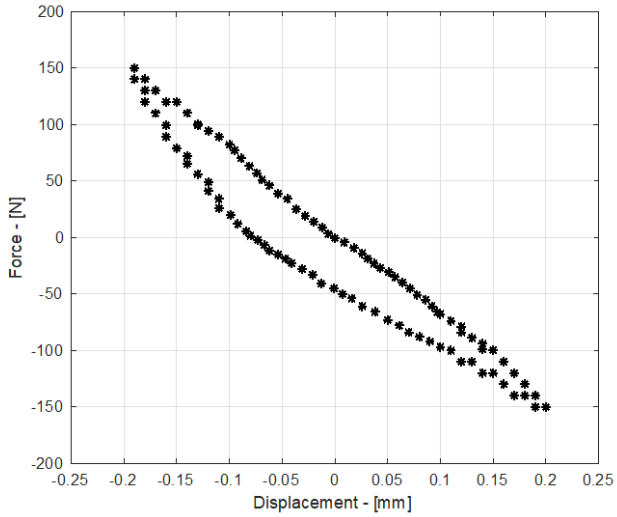

Figure 6 - Load-displacement curve of the foil bearing under investigation (back bearing).

Bearing Preload Estimation. Given the compliance of the GFJBs, the assembly clearance of the bearing is a murky concept. An alternative to the clearance is the preload, which is the pressure exerted on the rotor due to the GFJB assembly. As the rotor spins and pressure builds up inside the bearing, at a certain rotational speed, the pressure is sufficient to push away the top foil and a gas film is created. A large preload would ensure high rotordynamic stability [12,13], on the expense of thermal loss and seizure risks, and vice-versa.

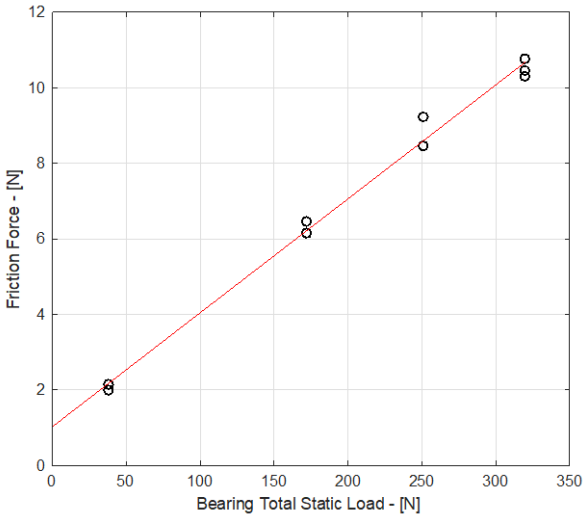

Figure 7 - Friction force versus static load used to quantify the bearing preload pressure.

DellaCorte et al. [14] suggested a procedure to estimate the preload pressure using break-away torque measurements at different static loads. The auxiliary break-away torque setup is used to perform this experiment. The experimental procedure starts with placing the bearing around a dummy rotor (same rotor diameter, and surface coating as the instrumented rotor), the bearing is then loaded statically using a deadweight. Consequently, the torque arm connected to the dummy rotor is gradually loaded. The force measured at the onset of the rotor's break-away multiplied by the length of the torque arm is the break-away torque for a given static load.

The slope of the friction force versus static load is the apparent friction coefficient. By extrapolation, the breakaway force at zero static load is the friction force. Dividing the friction force by the apparent friction coefficient yields an average normal preload force, which is circumferentially pressing the top foil against the rotor. Dividing the normal force by the bearing's circumferential area (perimeter x length), yields an average preload pressure.

The bearing under investigation was tested up to 319.5 N of static load. Figure 7 plots the friction force versus static load. The extrapolation yielded a friction force of 1.032 N at zero static load, and an apparent friction coefficient of 0.03. Hence, yielding a preload pressure of 6.85 kPa.

DYNAMIC RESPONSE OF INSTRUMENTED ROTOR

The running cycle starts from stationary conditions, ramping up to 37.5 krpm (linear ramp 0.005 s/rpm), cruising at speed, and free spinning down to stationary. Figure 8 presents a waterfall plot of the dynamic response of the rotor through the back bearing. Observing the waterfall plot, a clear synchronous amplitude is following the speed increase. The bearing exhibits a minute supersynchronous (2x, and 3x) vibrations. Some nearly negligible subsynchronous vibrations are present at a constant frequency that appears at 26 krpm, at a frequency of 135 Hz (0.31x).

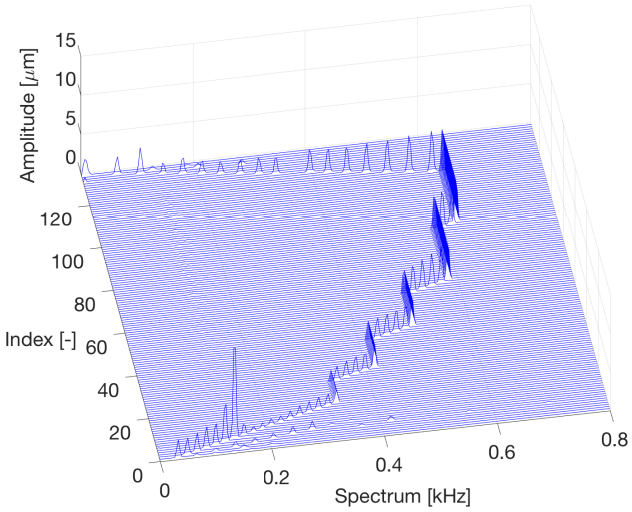

Figure 8 - Waterfall plot of the instrumented rotor response measured from the back foil bearing where the pressure measurement are executed. The rotor is driven through some intermediate cruising speeds to acquire data at steady-state conditions.

The synchronous dynamic response (peak-peak amplitude), and phase lag measured from the front (drive end) and back (non-drive end) bearings are presented in Figure 9. A large amplification due to resonance is observed at 9.3 krpm, beyond which no other critical speeds are encountered up to 37.5 krpm.

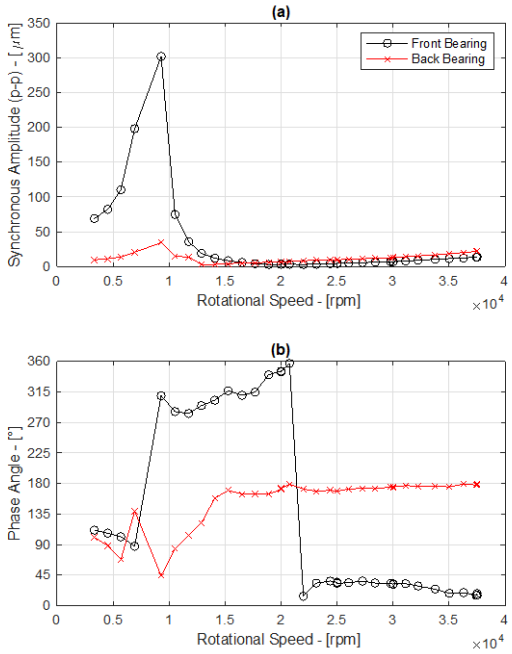

Figure 9 - Dynamic response of the instrumented rotor in terms of (a) peak-peak amplitude, and (b) phase lag measured from the front and back bearings.

STATIC ECCENTRICITY

The mean of the x-y proximity probes signal is interpreted as the static eccentricity of the rotor. The eccentricity is defined as the center of the rotor orbit normalized by the bearing clearance. In rigid bearings, this is usually done by measuring the minimum and maximum rotor travel within the bearing clearance using the x-y proximity probes. However, since foil bearings are compliant by nature, and the rotor can travel beyond the assembly clearance of the bearing, such technique is impossible. Therefore, the absolute distance between the center of the orbit and the proximity probe is measured, which can give an indication of the behavior of the eccentricity. The distance is measured relative to the stationary rotor position. Figure 10 shows the vertical and horizontal components measured during a coast down from 37.5 krpm to stationary conditions. The vertical component is measured below the rotor and opposite to the gravity load vector. It is observed that the rotor withdraws away from the probe towards the bearing center by 9.5 µm at maximum speed in an exponential trajectory. The horizontal component starts by abruptly withdrawing away from the probe by 9.7 µm at 4.8 krpm, then inflects and starts re-approaching the probe to remain at a distance of 4 µm at maximum speed. The observed rotor center trajectory as a function of speed matches basic theory of fluid film bearings [15].

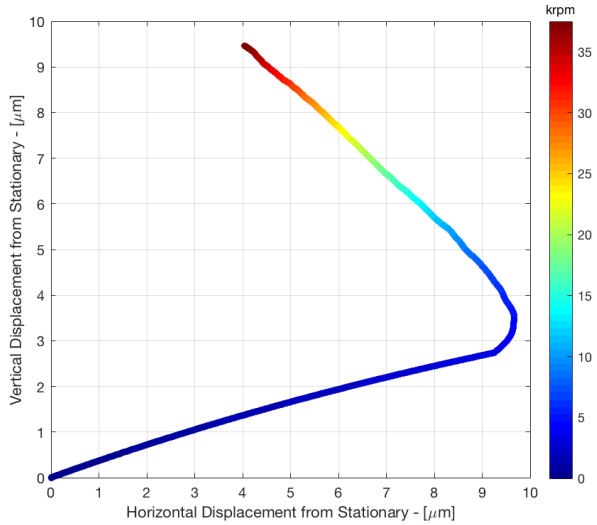

Figure 10 - Static rotor position at different speeds measured from the horizontal and vertical proximity probe placed below the rotor.

ROTOR ORBITS

The time-domain x-y signals of the proximity probes on the front (drive end) and back (non-drive end) GFJBs are used to deduce the rotor orbit. The signals are subjected to a lowpass filter with a cutoff frequency 5x of the fundamental (rotor speed). The mean is then subtracted from the filtered signals.

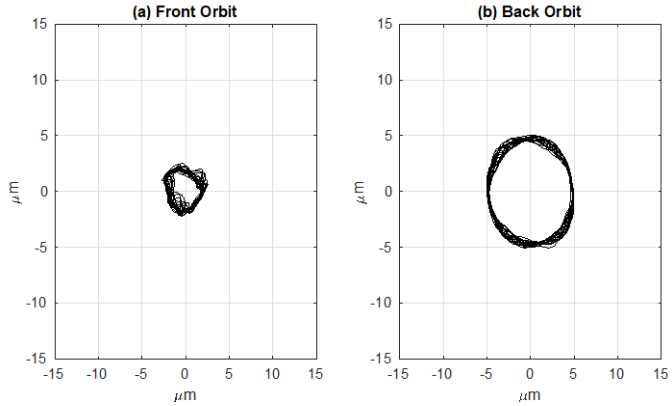

Figure 11 - Rotor orbits measured from the (a) front, and (b) back bearings at 25 krpm.

Figure 11 and Figure 12 show the orbits at the front and back bearings at 25 and 37.5 krpm respectively. The orbits were clear of any signs of subsynchronous vibrations, hence confirming the observations of the waterfall plots. The front bearing had smaller orbits

compared to the back bearing, which is a result of the imbalance response. The maximum orbit observed beyond resonance is of 20 µm at maximum speed of 37.5 krpm.

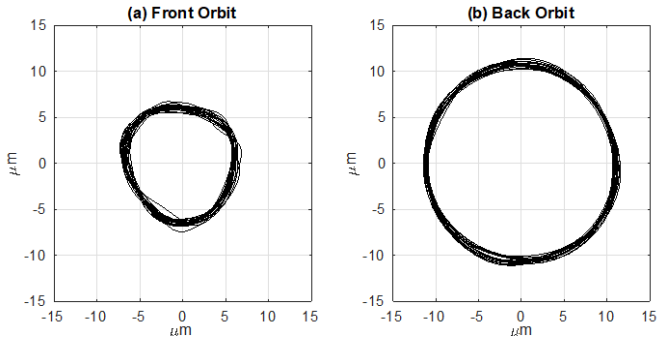

Figure 12 - Rotor orbits measured from the (a) front, and (b) back bearings at 37.5 krpm.

LIFTOFF SPEED IDENTIFICATION

The rotor liftoff speed is defined as the speed necessary to produce enough fluid film pressure to completely carry the rotor's weight, at which the friction torque inside the bearing is minimal. It also corresponds to the beginning of the hydrodynamic lubrication regime. As the current state of the test-rig does not allow the direct torque measurement, coast down tests are used to measure the minimum torque speeds. The rotor-bearing system is described as follows:

$$(J_{rot} + J_{mot} + J_{coup})\dot{\omega} = T_{FB} + T_{REB} + T_{windage} \qquad (1)$$

Where J_{rot} is the test rotor inertia, J_{mot} is the electric motor rotor inertia, J_{coup} is the coupling inertia, $\dot{\omega}$ system deceleration. T_{FB} is the friction torque of the two GFJBs, T_{REB} friction torque of the electric motor's roller element bearings, and $T_{windage}$ is the windage loss of the motor (windage losses of the test rotor are negligible). Rotor speed coast down is plotted versus time, and numerically differentiated producing the deceleration $\dot{\omega}$. The total rotor inertia is calculated from CAD. The product of the deceleration and the inertia yields the friction torque of the complete rotor assembly. Plotting the friction torque versus the corresponding rotational speed yields the Stribeck curve. However, and in order to identify the friction torque of the GFJBs alone (and the windage loss of the test rotor), the same coast down test is done for the electric motor alone and the equation of motion becomes:

$$J_{mot}\,\dot{\omega} = T_{REB} + T_{windage} \qquad (2)$$

Consequently, the roller element bearings friction torque and the windage losses inside the electric motor are quantified for the full operational speed range. T_{REB} and $T_{windage}$ are substituted into equation (1) to yield the friction torque of the two GFJBs.

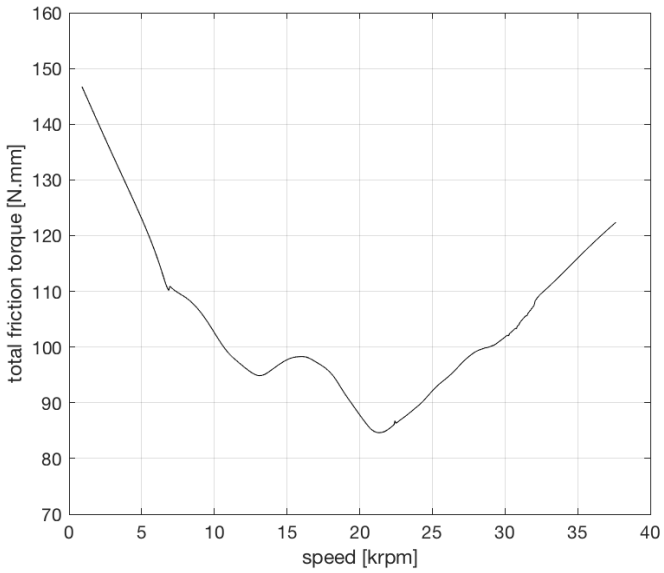

Figure 13 - Friction torque as a function of rotational speed.

Figure 13 shows the GFJBs friction torque versus the instrumented rotor speed. Two local minima are observed at 13.1 and 21.3 krpm, the two points corresponds to the liftoff speeds of the back and front bearings respectively. It is more challenging for the front bearing to liftoff due to the influence of the mechanical coupling in its vicinity.

GAS FILM PRESSURE MEASUREMENT

The fluid film pressure measurements are streamed and clocked simultaneously with the proximity measurements and the analog trigger signal. The pressures were measured at a constant light load (rotor weight), but at different rotational speeds up to 37.5 krpm. The pressure signals are ensemble averaged at steady state conditions. Following that, the raw signal is converted from volt to bar. Consequently, the signals are corrected for the effect of centrifugal force. The pressure measurement uncertainty is less than 1%.

The instrumented rotor was placed in a position where one probe is located at $\bar{z}$ = 0 (mid plane, 0.5L), and a second probe is located at $\bar{z}$ = -0.5 (0.75L). Figure 14 shows the measured pressure profiles at 15, 25, 30, and 37.5 krpm. The fluid film pressure is increasing with the rotational speed potentially due to the centrifugal growth of the rotor, as well as the increasing rotor orbit that grows by 120% between 20 krpm and 37.5 krpm. The pressure profiles at the bearing center are larger in magnitude than the profiles at $\bar{z}$ = -0.5 - Figure 15. The measured profiles are not adopting a smooth bell-shaped pressure profile as predicted by the available GFB models, probably due to the significant lack of circularity of the bearing under investigation. Instead, five pressure peaks are observed both at $\bar{z}$ = 0, and -0.5. The peaks in pressure match in position for the profiles measured at $\bar{z}$ = 0, and -0.5. Subambient pressure is observed only near the trailing edge of the top foil at 15, and 25 krpm.

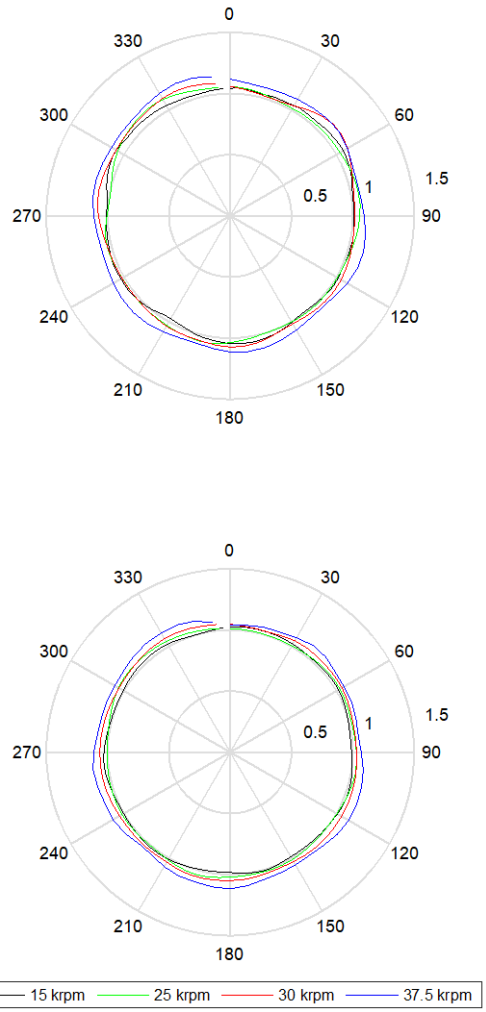

Figure 14 - GFJB pressure profiles measured at different rotational speeds at (a) $\bar{z}$ = 0, and (b) $\bar{z}$ = -0.5. Measurement uncertainty is less than 1%.

The two measured pressure profiles are used to estimate the bearing load. The profile measured at $\bar{z}$ = -0.5 is assumed to be equal to the profile at $\bar{z}$ = 0.5 (symmetric assumption). By integrating the pressure field over the bearing, a load of 6.8 N is estimated, which is approximately 70% of the fraction of rotor weight acting on the bearing. Given the large interpolations involved in this procedure, as well as the optimistic symmetric assumption, the result was found satisfactory.

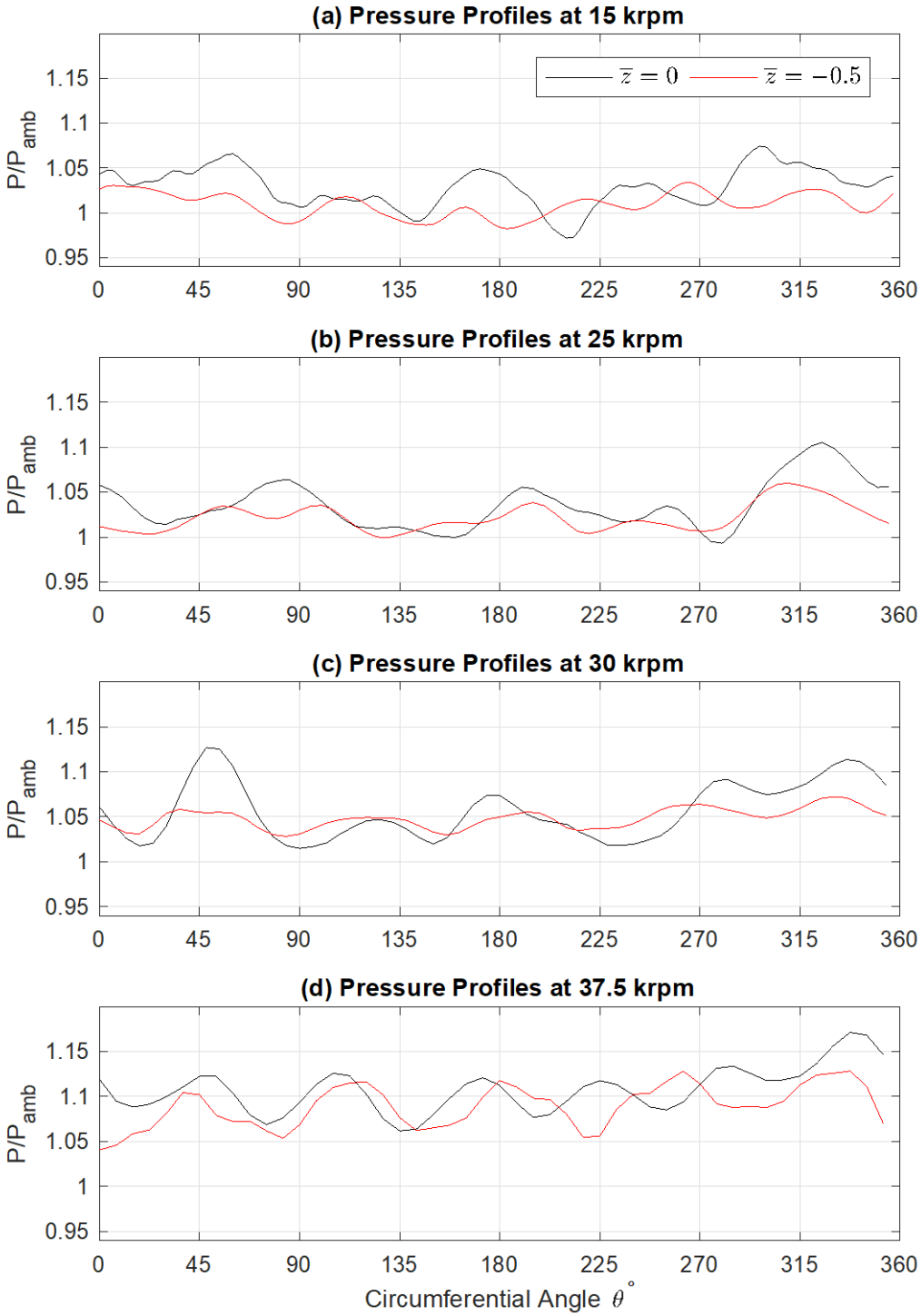

Figure 15 - Comparison of pressure profiles measured at z = 0, and -0.5 at different rotational speeds. Measurement uncertainty is less than 1%.

EXPERIMENTAL DATA AND MODEL COMPARISON

The foil bearing model proposed by Kim and San Andrés [16], and adopted by Schiffmann and Spakovszky [13] is being used to compare the estimated to the measured pressure profiles. The model adopts the frequency domain method, and solves the compressible Reynolds equation using the perturbation method of Lund [17]. The resulting partial differential equations are solved using the finite

element method of Faria and San Andrés [18] and Faria [19]. The bearing parameters simulated are summarized in Table 1. The model is also capable of simulating the effect of shimming (local disturbance of the circularity of the bearing).

Table 1 - Foil bearing model parameters.

Foil bearing parameters	
D [mm]	40
L/D [-]	1
C [μm]	30
$\boldsymbol{\alpha_{comp}}$ **[-]**	0.67
$\boldsymbol{\gamma}$ **[-]**	0.14
$\boldsymbol{R_D}$ **[mm]**	3.32
$\boldsymbol{\alpha_D}$ **[°]**	63.15
$\boldsymbol{t}$ **[mm]**	0.1

Comparing the measured and estimated pressure profiles at the bearing center - Figure 16, a clear mismatch is observed. The model's pressure profile is of a classic bell-shaped form, with the peak pressure towards the attitude angle. Based on the outcome of previous work by the authors [10], it is hypothesized that this apparent mismatch is a consequence of the geometrical deviations induced by the manufacturing process. This is also suggested by Figure 5. An attempt to match the measurements was executed using shimming patterns along the rotor circumference in order to disturb the bearing circularity. The result of the simulation highlights the potentials for qualitatively similar pressure profiles once the perfect circularity assumption is omitted - Figure 16. The shimming pattern is described as 9, 21, and 21 μm thick shims, at 40°, 270°, and 320° from the feedline. Similar estimated pressure profiles were presented by Kim and San Andres [12] for a shimmed (non-circular) GFJB.

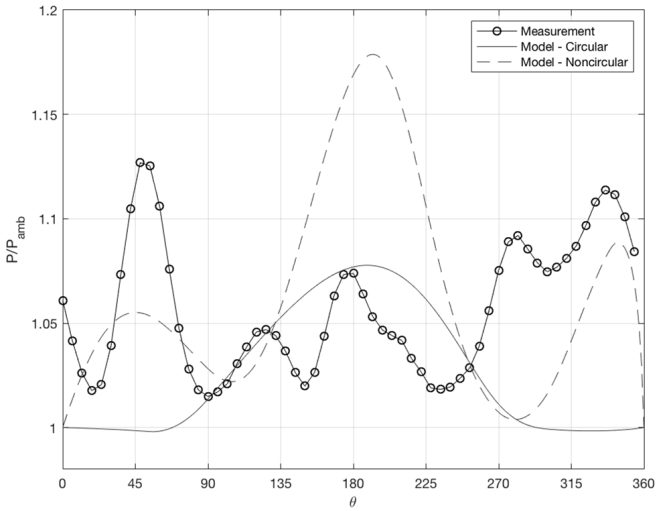

Figure 16 - Comparison of measured and modeled pressure profiles for circular and noncircular GFJBs. Measurement uncertainty is less than 1%.

Following that, it was decided to load the GFJBs during the pressure measurement. A simple foil under tension is wrapped around the rotor and pulled using the loading mechanism described in [10]. It is worth mentioning that such loading concept is the basis from which stemmed the compliant foil bearing technology. Such concept was first presented by Blok and vanRossum in 1953 [20]. Figure 17 shows a photograph of the loaded instrumented rotor.

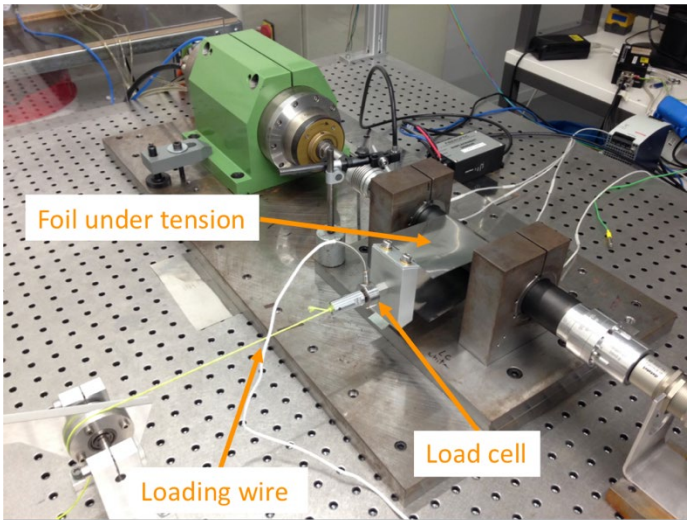

Figure 17- Photograph of the instrumented rotor supported on GFJBs and loaded using a simple foil under tension.

The test GFJB was loaded with 30 N, at 270º, while rotating at 35 krpm. The pressure profiles were measured at steady-state conditions. A pressure peak was observed at 280º. In a second attempt to validate the foil bearing model, a comparison is presented in Figure 18. It can be clearly observed that the model matches the pressure measurements with good accuracy only at the loaded region. Similar behavior was observed by several authors [8,21,22] in their attempt to validate their proposed models using the fluid film thickness measurement of Ruscitto et al.[6].

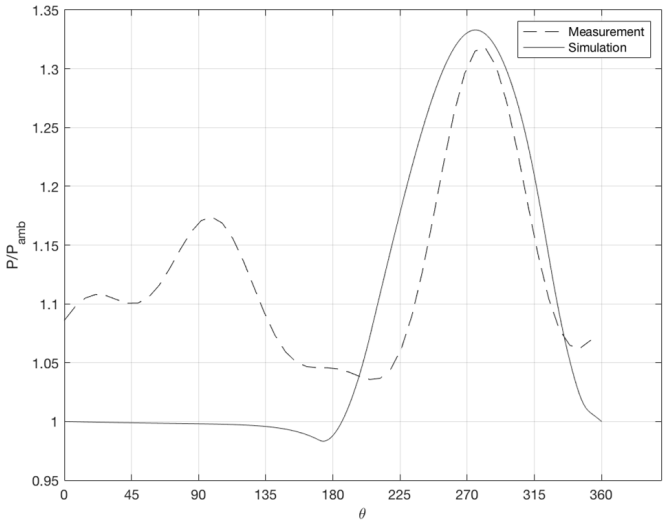

Figure 18 - Loaded pressure profile measured at 35 krpm and 30 N in the middle of the GFJB and compared to the model predicted pressure profile. Measurement uncertainty is less than 1%.

CONCLUSIONS

The paper presented results of an experimental measurement campaign on GFJBs using an instrumented rotor capable of measuring the pressure profiles within their gas film. The characteristics of the bearing under investigation were identified using geometrical measurements, load-displacement tests, and preload estimation. The rotordynamic response of the instrumented rotor supported on GFJBs highlighted the stable operation of the rotor, the critical speed at approximately 9 krpm, as well as the growing rotor orbit. The liftoff speed is estimated to be 21 and 13 krpm for the front and back bearings respectively.

The measured pressure profiles within the gas film are not adopting a classical bell-shaped profile at light loading condition (9 N). A comparison between the foil bearing model of Schiffmann and Spakovszky [13] highlighted large discrepancy between measurement and simulation at these conditions. After loading the bearing by 30 N at 35 krpm, the comparison between the model and the measurements were in a very good agreement at the loaded region of the bearing. It is concluded that given the nature of compliant foil

bearings, lightly loaded fluid film measurements are difficult to match using foil bearing models due to the high level of uncertainty resulting mainly from manufacturing and misalignment errors. The influence of such errors is less pronounced on the fluid film once the bearing is significantly loaded.

ACKNOWLEDGMENTS

This research was funded by the Swiss National Science Foundation (SNF Grant PYAPP2 154278/1). The authors would like to thank Mr. Guenat for his help in during the execution of loaded test.

REFERENCES

[1] Agrawal, G. L., 1997, "Foil Air/Gas Bearing Technology—an Overview," *ASME 1997 International Gas Turbine and Aeroengine Congress and Exhibition*, American Society of Mechanical Engineers, p. V001T04A006-V001T04A006.

[2] Heshmat, H., Tomaszewski, M. J., and Walton, I., James F., 2006, "Small Gas Turbine Engine Operating With High-Temperature Foil Bearings," pp. 387–393.

[3] Gu, A., 1994, "Cryogenic Foil Bearing Turbopumps," *32nd Aerospace Sciences Meeting and Exhibit*, American Institute of Aeronautics and Astronautics.

[4] Wade, J. L., Lubell, D. R., and Weissert, D., 2008, "Successful Oil-Free Version of a Gas Compressor Through Integrated Design of Foil Bearings," pp. 969–973.

[5] Lee, Y.-B., Bum Kwon, S., Kim, T. H., and Sim, K., 2013, "Feasibility Study of an Oil-Free Turbocharger Supported on Gas Foil Bearings Via On-Road Tests of a Two-Liter Class Diesel Vehicle," J. Eng. Gas Turbines Power, **135**(5), pp. 052701-052701–10.

[6] Ruscitto, D., McCormick, J., and Gray, S., 1978, "Hydrodynamic Air Lubricated Compliant Surface Bearing for an Automotive Gas Turbine Engine I-Journal Bearing Performance. NASA CR 135368," Natl. Aeronaut. Space Adm. Clevel. OH.

[7] Mai, T., 2015, "Technology Readiness Level," nasa.gov [Online]. Available: http://www.nasa.gov/directorates/heo/scan/engineering/technology/txt_accordion1.html. [Accessed: 05-Sep-2018].

[8] San Andrés, L., and Kim, T. H., 2009, "Analysis of Gas Foil Bearings Integrating FE Top Foil Models," Tribol. Int., **42**(1), pp. 111–120.

[9] Shalash, K., and Schiffmann, J., 2019, "An Instrumented High-Speed Rotor With Embedded Telemetry for the Continuous Spatial Pressure Profile Measurement in Gas Lubricated Bearings: A Proof of Concept," *ASME. Turbo Expo: Power for Land, Sea, and Air*, Phoenix, AZ, USA.

[10] Shalash, K., and Schiffmann, J., 2017, "Comparative Evaluation of Foil Bearings With Different Compliant Structures for Improved Manufacturability," *ASME. Turbo Expo: Power for Land, Sea, and Air*, ASME, Charlotte, NC, USA, p. V07AT34A014.

[11] Shalash, K., and Schiffmann, J., 2017, "On the Manufacturing of Compliant Foil Bearings," J. Manuf. Process., **25**, pp. 357–368.

[12] Kim, T. H., and Andrés, L. S., 2009, "Effects of a Mechanical Preload on the Dynamic Force Response of Gas Foil Bearings: Measurements and Model Predictions," Tribol. Trans., **52**(4), pp. 569–580.

[13] Schiffmann, J., and Spakovszky, Z. S., 2012, "Foil Bearing Design Guidelines for Improved Stability," J. Tribol., **135**(1), pp. 011103–011103.

[14] DellaCorte, C. L., 2000, *Performance and Durability of High Temperature Foil Air Bearings for Oil-Free Turbomachinery*.

[15] Fuller, D. D., 1969, "A Review of the State-of-the-Art for the Design of Self-Acting Gas-Lubricated Bearings," J. Lubr. Technol., **91**(1), pp. 1–16.

[16] Kim, T. H., and San Andrés, L., 2008, "Heavily Loaded Gas Foil Bearings: A Model Anchored to Test Data," J. Eng. Gas Turbines Power, **130**(1), pp. 012504–012504.

[17] Lund, J. W., 1968, "Calculation of Stiffness and Damping Properties of Gas Bearings," J. Lubr. Technol., **90**(4), pp. 793–803.

[18] Faria, M. T. C., and Andrés, L. S., 1999, "On the Numerical Modeling of High-Speed Hydrodynamic Gas Bearings," J. Tribol., **122**(1), pp. 124–130.

[19] Faria, M. T. C., 2001, "Some Performance Characteristics of High Speed Gas Lubricated Herringbone Groove Journal Bearings," JSME Int. J. Ser. C Mech. Syst. Mach. Elem. Manuf., **44**(3), pp. 775–781.

[20] Blok, H., and vanRossum, J., 1953, "The Foil Bearing-a New Departure in Hydrodynamic Lubrication," Lubr Eng, **9(6)**, pp. 316–20.

[21] Lee, D.-H., Kim, Y.-C., and Kim, K.-W., 2008, "The Static Performance Analysis of Foil Journal Bearings Considering Three-Dimensional Shape of the Foil Structure," J. Tribol., **130**(3), pp. 031102-031102–10.

[22] Feng, K., and Kaneko, S., 2010, "Analytical Model of Bump-Type Foil Bearings Using a Link-Spring Structure and a Finite-Element Shell Model," J. Tribol., **132**(2), pp. 021706-021706–11.